Article

Entropy-increased $LiMn_2O_4$-based positive electrodes for fast-charging lithium metal batteries

Weihao Zeng[1,3], Fanjie Xia[1,3], Juan Wang[1,3], Jinlong Yang[2,3], Haoyang Peng[1,3], Wei Shu[1], Quan Li[1], Hong Wang[1], Guan Wang[1], Shichun Mu[1] ✉ & Jinsong Wu[1] ✉

Fast-charging, non-aqueous lithium-based batteries are desired for practical applications. In this regard, $LiMn_2O_4$ is considered an appealing positive electrode active material because of its favourable ionic diffusivity due to the presence of three-dimensional Li-ion diffusion channels. However, $LiMn_2O_4$ exhibits inadequate rate capabilities and rapid structural degradation at high currents. To circumvent these issues, here we introduce quintuple low-valence cations to increase the entropy of $LiMn_2O_4$. As a result, the entropy-increased $LiMn_2O_4$-based material, i.e., $LiMn_{1.9}Cu_{0.02}Mg_{0.02}Fe_{0.02}Zn_{0.02}Ni_{0.02}O_4$, when tested in non-aqueous lithium metal coin cell configuration, enable 1000 cell cycles at $1.48\,A\,g^{-1}$ (corresponding to a cell charging time of 4 minutes) and 25°C with a discharge capacity retention of about 80%. We demonstrate that the increased entropy in $LiMn_2O_4$ leads to an increase in the disordering of dopant cations and a contracted local structure, where the enlarged LiO_4 space and enhanced Mn-O covalency improve the Li-ion transport and stabilize the diffusion channels. We also prove that stress caused by cycling at a high cell state of charge is relieved through elastic deformation via a solid-solution transition, thus avoiding structural degradation upon prolonged cycling.

Extreme fast charging (XFC) aims to charge a fully discharged non-aqueous Li-based battery up to 80% of its total capacity in about 10–15 min, which is about 3–5 times faster than conventional fast charging[1,2]. To operate in XFC conditions, a non-aqueous Li-based battery requires electrode material with high electronic and ionic conductivity[3]. The enhancement of Li$^+$ ion diffusion is particularly important since ionic diffusivity, which is usually slower than electron transport, is an essential factor for electrode active materials in XFC non-aqueous Li-based batteries[4,5]. From an atomic perspective, there should be interlinked cation vacancies with a relatively low energy barrier for Li$^+$ migration, and the Li$^+$ diffusion channels should remain stable through multiple cycles of lithiation and delithiation[6]. As such, intercalation-type positive electrode active materials are the choice for

XFC non-aqueous Li-based batteries, since they can sustain the stability of the framework structure during electrochemical reactions. In this regard, we focused our attention on three main intercalation-type positive electrode active materials which are commercially available: olivine structure $LiFePO_4$, layered structure $LiCoO_2$ and $LiNi_xCo_yMn_{1-x-y}O_2$, and spinel $LiMn_2O_4$ (LMO). Among them, the spinel LMO, which is both low-cost and environmentally-friendly[7,8], is among the positive electrode active materials that have the highest ionic diffusivity, due to the presence of three-dimensional Li-ion diffusion channels. Each Li$^+$ in the LiO_4 tetrahedron is surrounded and face-shared by four octahedral vacancies[8,9], which allows a low energy barrier for Li$^+$ to diffuse along the channel, rendering the spinel structure an ideal choice for high ionic diffusivity[10,11].

[1]State Key Laboratory of Advanced Technology for Materials Synthesis and Processing, Wuhan University of Technology, Wuhan, Hubei, China. [2]Guangdong Research Center for Interfacial Engineering of Functional Materials, Shenzhen University, Shenzhen, China. [3]These authors contributed equally: Weihao Zeng, Fanjie Xia, Juan Wang, Jinlong Yang, Haoyang Peng. ✉e-mail: msc@whut.edu.cn; wujs@whut.edu.cn

However, spinel LMO falls short to meet the requirement of XFC non-aqueous Li-based batteries, as it exhibits a rapid capacity fading when operated at high current rates (e.g. >740 mA g⁻¹)[12]. Despite the presence of 3D channels for Li⁺-ions diffusion, the mechanism which causes inadequate rate capabilities performance for LMO-containing non-aqueous Li-based cells for the XFC applications remains unclear. In general, to increase the amount of Li⁺-ions reversibly intercalated and extracted in a shorter time, the ionic diffusion rate must be enhanced to facilitate fast Li⁺-ions migration[13,14]. Meanwhile, to reduce capacity fading, the 3D diffusion channels in LMO (atomic sites of 8a-16d-8a in the spinel structure) need to remain undisturbed when experiencing the stress caused by lattice expansion and contraction during electrochemical lithiation and delithiation[15]. However, when a large coordination evolution occurs, such as massive migration of atoms, the diffusion channels become blocked, leading to a decline in the mobility of Li⁺ ions[16,17]. High entropy engineering has been demonstrated to be an effective approach to improve mechanical properties of materials through entropy stabilization[18,19]. Specifically, several high-entropy positive electrode active materials, such as with disordered rocksalt structures[20], and layered structures[21], enable non-aqueous Li-based cells with high rate capability. A recent theoretical study has also shown the diffusion barrier can be lowered due to the overlapping distribution of site energies, thereby increasing the ionic conductivity of Li⁺-ion solid electrolytes when high-entropy metal cations are mixed[22]. We thus hypothesize that using an increased entropy strategy, we could design LMO-based positive electrode active materials for developing XFC non-aqueous Li-based batteries.

In this work, by adjusting the number of cationic doping, we have successfully synthesized a single-phase spinel $LiMn_{1.9}Cu_{0.02}Mg_{0.02}Fe_{0.02}Zn_{0.02}Ni_{0.02}O_4$ (denoted as EI-LMO for entropy-increased LMO) with an increased entropy of $0.28R$ (R is Avogadro constant, the entropy calculation is presented in Supplementary Note 1)[23]. EI-LMO, used as positive electrode active material in non-aqueous lithium metal batteries in coin cell configuration, deliver a specific discharge capacity of 94.7 mAh g⁻¹ at 1.48 A g⁻¹, which is 80.4% of the capacity achieved at 14.8 mA g⁻¹. Additionally, it maintains 80% of its capacity at 1.48 A g⁻¹ and 25°C after 1000 cycles. The Mn-rich structure and capacity at the potential of ~4.1 V in LMO are well maintained through the increased-entropy strategy, with the fixed dopant concentration of 5 at% (see Supplementary Table 1)[24–33]. We have observed in LMO a plastic deformation in the form of high-density stacking faults, coincided with the sharp drop of Li⁺-ion diffusivity, making LMO unsuitable for extreme fast charging. In contrast, with slightly increased entropy of $0.28R$, the EI-LMO shows an elastic deformation and solid-solution transformation even at high charging state, maintaining the 3D diffusion channels and fast Li-ion diffusion kinetics, and avoiding formation of defects and structure degradation during battery cycling in lithium metal coin cell configuration.

Results and Discussion
Rational design of dopant elements
In order to find appropriate dopant cations capable of enhancing diffusion kinetics and improving structural stability, a systematical simulation was undertaken using density functional theory (DFT) and Nudged Elastic Band (NEB) computations to probe the impacts and functions of various doping elements on the local structure of LMO lattices. The nine cationic elements (Mg, Al, Ti, V, Cr, Fe, Ni, Cu, Zn) are selected from the period table (Supplementary Figs. 1-2) and individually incorporated into LMO lattices of $1 \times 1 \times 2$ supercells through the substitution of four Mn atoms (termed as Mg-LMO, Al-LMO, Ti-LMO, V-LMO, Cr-LMO, Fe-LMO, Ni-LMO, Cu-LMO, Zn-LMO). Together with undoped LMO, as depicted in Fig. 1a, the ten structures can be categorized into three groups. The first group contains LMO, Cr-LMO, Al-LMO, and V-LMO, where the changes in their local structures (Mn-O and M-O bonds) due to the doping are small. The second group,

Ti-LMO with substitution of Mn by the high-valence metal element Ti, displays significant alterations in the local structure, showing the elongated Ti-O bond and increased Mn-O bond. The third group, consisting of low-valence metal elements like Cu, Mg, Fe, Zn and Ni, induces the elongated M-O bond, the shortened Mn-O bond and the elongated Li-O bond.

The impacts of various dopant cations on local structures stem from disparities in electron interactions between these ions and the coordinated oxygen (M-O), as well as the interactions between Mn and oxygen (Mn-O). As shown in Fig. 1b-d, the 2D contour plots of Electron Localization Function (ELF) of LMO, Ti-LMO, and Cu-LMO, along with the Bader charge value on each atom, demonstrate the three types of the local structures. In these structures, the bond length (M-O), adjacent Li-O distance, and Mn-O bond length are changed by the doped cations due to their different abilities to localize electron, which are identified by the Bader charge value. Taking Mn as an example, the Bader charge of each Mn is consistent, indicating that the charge transfer between each Mn atom and O atoms is uniform. The Bader charge values of Cr, Al, and V are in close proximity to that of Mn; therefore, the charge transfer process can also be disregarded in Cr, Al, and V-doped structures. In comparison, Ti enables Mn atoms to transfer charges to Ti through O atoms, leading to the reduction of Mn's oxidation state and elongated Mn-O bond length. This is confirmed by the significantly smaller Bader charge of Ti compared to adjacent Mn. Meanwhile, Cu can trigger a charge transfer from Cu to Mn atoms via O atoms, showing the electron delocalization capability. Such a charge transferring process fortifies the Mn-O bond and raises the oxidation state of Mn. The other four elements, Mg, Fe, Zn, and Ni, have similar properties as Cu, as evidenced by the ELF of valence electrons projected along the (100) lattice planes (Supplementary Fig. 3). The bond length (M-O), Li-O bond and Mn-O bond across the ten lattices, is elucidated in Figs. 1e and 1f. The introduction of Cu, Mg, Fe, Zn, and Ni cations results in the largest increases in M-O bond lengths and Li-O distances, coupled with the most substantial reduction in Mn-O bond lengths. Theoretically, the increased Li-O distance can weaken the electrostatic interaction between Li and O, thereby facilitating Li⁺ diffusion and stabilizing the 3D diffusion channels.

As three representatives of various cation-doped configurations, LMO, Ti-LMO and Cu-LMO were further investigated via NEB calculations to elucidate the Li⁺ diffusion pathways and associated barriers. Within LMO, as depicted in Fig. 1g, the pathway for Li⁺ migration from tetrahedral sites (8a) to octahedral interstitials (16c) and then to subsequent tetrahedral sites exhibits a high degree of symmetry. In Ti-LMO (Fig. 1h), the diffusion of Li⁺ leads to a geometric displacement away from Ti. This is ascribed to the electron localization effect of Ti, which consequently alters the electrostatic interaction and distance between Li⁺ and O. Conversely, in Cu-LMO (Fig.1i), the diffusion of Li⁺ along the 8a-to-16c pathway triggers off-centering towards Cu. This is a result of the electron delocalization effect of Cu, which influences the electrostatic interaction between O and Li. At the 8a site, the Li-O distance in LMO is 1.937 Å. In Ti-LMO, it is divided into 1.954 and 1.925 Å, with the latter being smaller than that in LMO. In Cu-LMO, the Li-O distance is divided into 1.985 to 2.005 Å, both values exceeding those observed in LMO, thus facilitating Li⁺ migration. As shown in Fig. 1j, NEB calculations reveal that, a significant rise in the diffusion barrier for Li⁺ in the Ti-LMO structure, while a notable drop is evident in Cu-LMO. Consequently, the introduction of Cu atoms has the effects of reducing the Li⁺ diffusion barrier and enhancing the stability of the 3D ion diffusion pathway. Similarly, Mg, Fe, Zn, and Ni, share similar characteristics with Cu, also suggesting a possible improvement for non-aqueous Li-ion storage at high currents.

Entropy-driven formation of cation-disordered structure
Based on the theoretical simulations, a series of LMOs including the undoped $LiMn_2O_4$ (LMO), single-cation doped LMOs
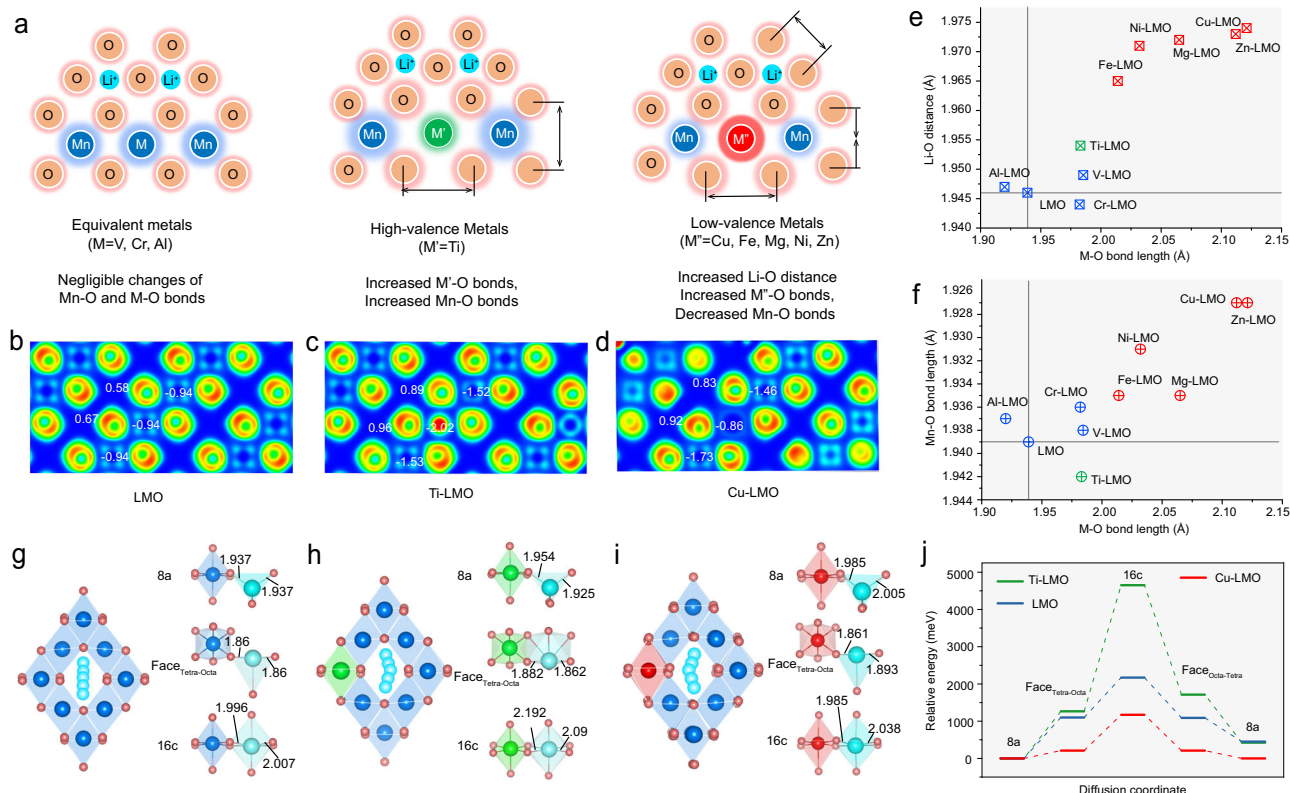
Fig. 1 | Local structures and diffusion barriers for elemental dopants in LMO. a Schematic illustrations of undoped and V, Cr, Al-doped LMO structure showing small changes, Ti-doped LMO structure showing expansion, and Cu, Fe, Mg, Ni, Zn-doped LMO structure showing contraction. The cyan, navy blue, emerald green, red, and sandy-brown spheres symbolize Li, Mn, and their equivalent metals (V, Cr, Al), a high-valence metal (Ti), low-valence metals (Cu, Fe, Mg, Ni, Zn) and O atoms, respectively. The shadows surrounding each sphere illustrate the varying electron localization capabilities among these different types of atoms. **b**–**d** 2D slices of electron localization function (ELF) of valence electrons viewed along the (100) lattice planes of **b** LMO, **c** Ti-LMO, **d** Cu-LMO, respectively. The numbers on the ELF contours are the calculated Bader charge values of O, Mn, Cu and Ti. **e**, **f** Impact of the M-O bond length on **e** Li-O distances and **f** Mn-O bond lengths in the ten structurally optimized LMO with different substituted cations, including Cu, Fe, Mg, Zn-doped LMO (red squares and spots), Ti-LMO (emerald green square and spot), and LMO doped with Mn, V, Cr, and Al (navy blue squares and spots). **g**–**i** Diffusion paths and Li-O bond length changes in **g** LMO, **h** Ti-LMO, and **i** Cu-LMO, respectively. The marked numbers are the bond length in Å. **j** Diffusion barriers of tetrahedron (8a)-octahedron (16c)-tetrahedron (8a) paths in LMO, Ti-LMO and Cu-LMO.

($LiMn_{1.9}M_{0.1}O_4$, M=Cu, Mg, Fe, Zn or Ni), and the five-cations doped $LiMn_{1.9}Cu_{0.02}Mg_{0.02}Fe_{0.02}Zn_{0.02}Ni_{0.02}O_4$ (EI-LMO) have been successfully synthesized via a facial solid-state reaction. As the number of doping cations increases from 0 to 1 and then to 5, the entropy value increases from 0 to 0.2 R and then to 0.28R[23]. The crystallographic structures of LMO and EI-LMO have been characterized by X-ray diffraction (XRD) measurements and Rietveld refinements (Supplementary Fig. 4 and Supplementary Tables 2-3). These results indicate the successful synthesis of EI-LMO, possessing the same space group as LMO (*Fd-3m*). The lattice parameter (a = 8.199 Å) of EI-LMO is smaller than that of LMO (a = 8.238 Å), with those of single-cation doped LMOs fall in between (Fig. 2a). There is a negative correlation between the lattice volume of LMOs and the increase in configuration entropy. Lattice parameters of the singly cation-doped samples are determined, which are in agreement with the simulations (Fig. 1f). For example, the lattice contraction observed in Cu-LMO, Fe-LMO, Mg-LMO, Zn-LMO, and Ni-LMO is due to the reduction of Mn-O bond lengths in the structures caused by the element doping, agreed with the simulations. It should be noted that additional lattice contraction is observed by simultaneously introducing five elements, which is an experimental proof of the increased entropy effect. Meanwhile, the LMO particles with increased entropy exhibit larger average sizes (Supplementary

Fig. 5). This may be attributed to the low eutectic effect arising from the multiple doping components[34].

As depicted in Fig. 2b, singly doped samples show localized cation ordering, possibly due to significant differences in radii between the doped ions and $Mn^{3.5+}$ ions. The effects of various cations (including Cu^{2+}, Mg^{2+}, Fe^{2+}, Zn^{2+}, Ni^{2+}) on the local structure are similar. Introducing more elements increases entropy, disrupts ordered arrangement of the cations and promotes the formation of the disordered structure. Supplementary Fig. 6 illustrates that as entropy increases, the disordered distribution of doping elements is promoted. In Fig. 2c, weak and diffused superlattice spots are observed in the selected area electron diffraction (SAED) patterns of Cu-LMO, Fe-LMO, Mg-LMO, Zn-LMO, and Ni-LMO, showing the appearance of localized and ordered structure. With entropy increased to 0.23 R, LMO co-doped with Cu, Fe (CuFe-LMO) presents the absence of this superlattice superstructure in the SAED pattern (Fig. 2d), yet faint superlattice rings are still visible in the nanoscale fast Fourier transformation (FFT) patterns (Fig. 2e). This suggests a decline in cation ordering when the number of the doped cations is doubled. Further increasing entropy to 0.28 R in EI-LMO results in the absence of superlattice signals in both SAED and FFT patterns (Fig. 2f, g), indicating a disordered distribution of the cations.

In EI-LMO, the five doped elements are uniformly distributed throughout the particles, as indicated by X-ray energy dispersive spectrum (EDS) mapping (Fig. 2h). The elemental signals of Cu, Fe, Mg,
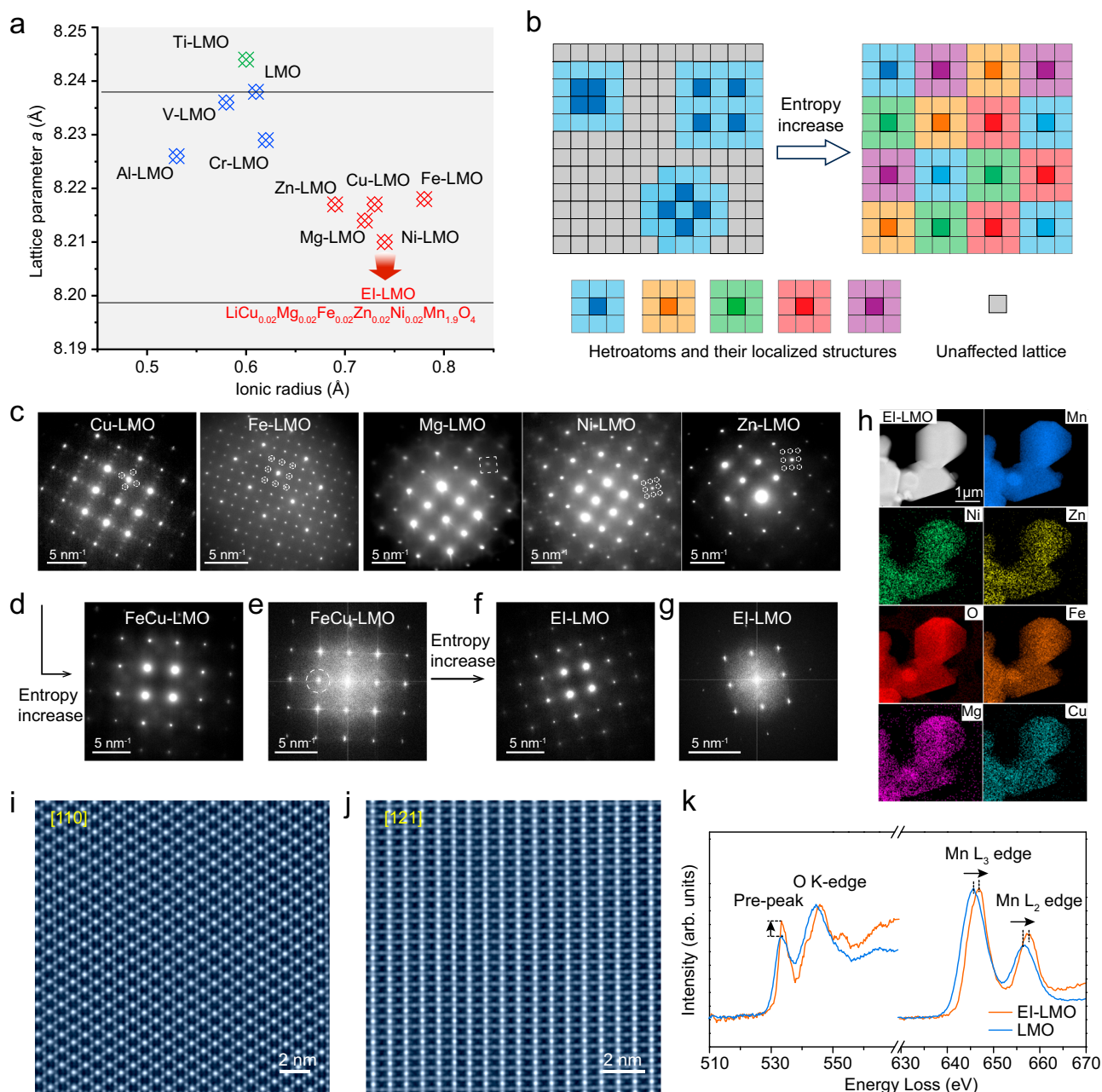
Fig. 2 | Characterizations of lattice structures and analysis of Mn valence and Mn-O hybridization in the pristine samples. a Correlation between the radii of the doped cations and the refined cell parameters observed in the synthesized LMOs. These include LMOs doped singly with Cu, Fe, Mg, Ni, and Zn (red spots), LMO singly doped with Ti (emerald green spot), LMOs singly doped with Mn, V, Cr, and Al (navy blue spots), and the EI-LMO (the gray horizontal line). **b** Schematic illustrations of the increased cation disorder in LMO structure with the increased entropy. Blue, yellow, green, red and purple squares and the lighter-colored squares illustrate the different doped atoms and the surrounding affected lattice (Heteroatoms and their localized structures). The gray squares illustrate the lattice regions that remain unaffected (Unaffected lattice). **c** SAED patterns of Cu-LMO, Fe-LMO, Mg-LMO, Zn-LMO, and Ni-LMO along the [100] axis. The dotted circles and dotted squares represent the diffraction spots and streaks of superstructure. **d**, **e** SAED **d** and FFT **e** patterns of CuFe-LMO. **f**, **g** SAED **f** and FFT **g** patterns of EI-LMO. **h** Element mappings of EI-LMO sample, including Mn, Ni, Zn, O, Fe, Mg and Cu. **i**, **j** HAADF STEM images of EI-LMO projected along the [110] axis (**i**) and [121] axis **j**, respectively. **k** Comparison of EELS spectra covering O K-edge and Mn L-edge between EI-LMO and LMO. The spectra are normalized to the zero-loss peak.

Zn and Ni can also be detected by X-ray photoelectron spectroscopy (XPS) in Supplementary Fig. 7. And the elemental distribution in singly cation-doped samples can be found in Supplementary Fig. 8. As revealed in the atomic-resolution high-angle annular dark field (HAADF) scanning transmission electron microscopy (STEM) image of the EI-LMO along the [110] zone axis (Fig. 2i), all of heavy metal atoms, including the doping elements and Mn, are mainly located at the 16d site. Atomic-level EDS mapping (Supplementary Fig. 9) with the doped concentration of ~1 at% presents a challenge. By elevating the

concentration of each dopant element to ~5 at%, we observed Cu, Fe, Mg, Zn, and Ni co-occupied the 16d sites with Mn, while the 16c sites remained vacant. This observation validates the occupancy of the 16d sites by the doped ions in EI-LMO. Observation along the [121] zone axis, which is the most advantageous direction for visualizing the diffusion channels in the spinel structure, confirms the 16c sites are empty, as shown in Fig. 2j. The electron diffraction patterns of the EI-LMO along the two different zone axes (Supplementary Fig. 10) confirm that the EI-LMO maintains the spinel structure. Comparing the
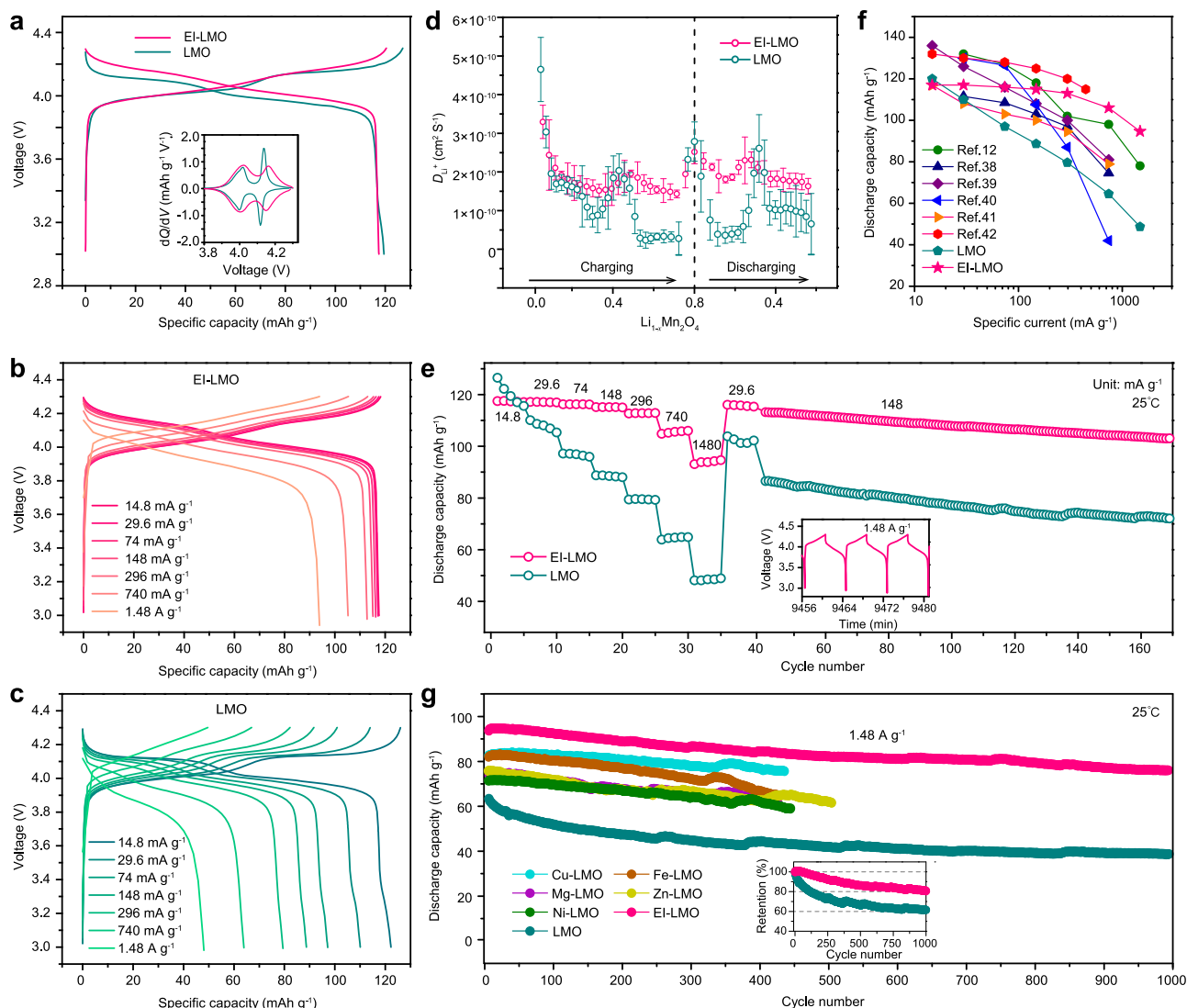
Fig. 3 | Li-ion storage properties on EI-LMO-based electrodes in Li metal coin cell configuration. a Charge and discharge curves of EI-LMO and LMO during the first cycle at 14.8 mA g⁻¹. The inset is the corresponding dQ/dV curves. **b**, **c** Charge and discharge curves of EI-LMO **b** and LMO **c** under various specific currents, spanning from 14.8 mA g⁻¹ to 1.48 A g⁻¹. These profiles are extracted from the same coin cell during its cycling at 25 °C, specifically from the 2nd, 7th, 12th, 17th, 22nd, 27th, and 32nd cycles, which correspond to specific currents of 14.8 mA g⁻¹, 29.6 mA g⁻¹, 74 mA g⁻¹, 148 mA g⁻¹, 296 mA g⁻¹, 740 mA g⁻¹ and 1.48 A g⁻¹, respectively. **d** Li⁺ diffusion coefficients of EI-LMO and LMO. These were calculated from the GITT results tested at 25 °C. Error bars represent standard deviations. **e** Rate performance of EI-LMO and LMO. The inset is the voltage-time plot of EI-LMO at 1.48 A g⁻¹ and 25 °C. Supplementary Fig. 14e displays the Coulombic efficiency that corresponds to the data presented in **e**. **f** Comparing the capacity of EI-LMO and LMO obtained at various specific currents with optimized rate performance reported in the recent literatures[12,38–42]. **g** Comparison of the long-term cycling performance at 1.48 A g⁻¹ and 25 °C between the series of the LMOs samples doped with diverse cation elements. The inset presents the capacity retention of LMO and EI-LMO at 1.48 A g⁻¹ and 25 °C over 1000 cycles. Supplementary Fig. 14c displays the Coulombic efficiency that corresponds to the data presented in **g**.

electron energy loss spectroscopy (EELS) spectra of EI-LMO and LMO (Fig. 2k), a rightward shift in the Mn L-edge of EI-LMO is found, which is attributed to a slight increase in the Mn-ion's valence. The change in the valence of Mn-ions is further supported by Mn 3s the XPS result as shown in Supplementary Fig. 11. We also observe an increase in the O pre-peak EELS, which results from the transition from O 1s state to a hybridized O 2p and Mn 3d states[35]. It indicates a highly hybridized Mn-O bonding with a decrease in the Mn-O bond distance and an increase in bond strength[36].

Testing of EI-LMO-based electrodes in non-aqueous lithium metal coin cell configuration

The Li-ion storage performance of EI-LMO and LMO as positive electrode active materials was evaluated in non-aqueous Li metal coin cell configuration. The cells containing the EI-LMO-based electrodes had a

higher Li⁺-ion rate capability than cells containing the LMO-based positive electrodes when subjected to extremely fast charge (the current value is above 592 mA g⁻¹). Their performance was initially measured and compared at a low specific current. At 14.8 mA g⁻¹ and 25 °C, the cell with the EI-LMO-based electrode exhibits a discharge capacity of 117 mAh g⁻¹ within the voltage window of 3–4.3 V in the first cycle, close to 120 mAh g⁻¹ of LMO (Fig. 3a). Interestingly, the voltage profile of the cell with the EI-LMO-based electrode exhibits a single-sloped voltage curve, in contrast to the two voltage plateaus typically observed in the cell with the LMO-based electrode. The single-slope feature corresponds to an increase in area intensity between 4.0 V and 4.1 V in the dQ/dV curve of the cell with the EI-LMO-based electrode (inset in Fig. 3a). Increasing the specific currents, the cell with the EI-LMO-based electrode can deliver capacities of 117, 116, 115, 113, 106 and 94.7 mAh g⁻¹ at 29.6 mA g⁻¹, 74 mA g⁻¹, 148 mA g⁻¹, 296 mA g⁻¹, 740 mA g⁻¹

and 1.48 A g⁻¹, respectively (Fig. 3b). Whereas, the cells with the LMO-based electrodes enable the capacities of 110, 97, 88.7, 79.6, 64.5 and 48.7 mAh g⁻¹ at 29.6 mA g⁻¹, 74 mA g⁻¹, 148 mA g⁻¹, 296 mA g⁻¹, 740 mA g⁻¹ and 1.48 A g⁻¹, respectively (Fig. 3c). The difference in specific discharge capacity between the cells containing the EI-LMO and LMO electrodes is more evident at the highest specific current. In particular, at the highest specific current, i.e., 1.48 A g⁻¹, the cell with the EI-LMO-based electrode delivers a specific discharge capacity almost double than the one with the LMO electrode.

The ionic diffusion kinetics was further investigated by the galvanostatic intermittent titration technique (GITT) test (Supplementary Fig. 12), and the variation of the Li-ion diffusion coefficient (D_{Li}^+) with the extraction and insertion of lithium ions was acquired (Fig. 3d and Supplementary Note 2). In LMO-based electrode, when Li is extracted above 0.5 per formula at the high-voltage plateau, the diffusivity of LMO drops largely, which is the major cause of the sluggish ionic diffusion[16,17]. Differently, the EI-LMO-based electrode exhibits a stable and high Li-ion diffusion coefficient in the whole cycle. Over 300 cycles, the diffusion coefficient remains stable in EI-LMO-based electrodes, as qualitatively evaluated by electrochemical impedance spectroscopy (EIS) measurement (Supplementary Fig. 13). Supplementary Fig. 14 reports the non-aqueous Li metal coin cells testing using LMO-based electrodes with different entropy levels. It can be seen that the multiplicity of doping elements, rather than the variety of elements, has an influence on the improvement of rate performance. Notably, in Li metal coin cells with the EI-LMO-based electrodes, the specific discharge capacity achieved at 1.48 A g⁻¹ is 80.4% of the one achieved at 14.8 mA g⁻¹ (Fig. 3b and Fig. 3e), thus, confirming the possible use of EI-LMO as positive electrode active material for XFC non-aqueous Li metal batteries[6,37]. This shows that a non-aqueous Li metal coin cell containing the EI-LMO-based positive electrode can be charged to 80% of its full capacity in about 4 minutes (see the inset of Fig. 3e). The graph in Fig. 3f discloses the comparison of the Li metal cells equipped with the EI-LMO-based electrode with other Li metal cells reported in the literature that uses LMO-modified positive electrodes[12,38–42]. The Li metal coin cells with the EI-LMO-based positive electrode tested for 1000 cycles at 1.48 A g⁻¹ (Fig. 3g) shows a discharge capacity retention of about 80.3% corresponding to a final discharge capacity of 75.5 mAh g⁻¹. Interestingly, the Li metal cell with the LMO-based positive electrode tested for 1000 cycles at the same high current shows a discharge capacity retention of about 61.3%, corresponding to a final discharge capacity of 39.9 mAh g⁻¹. In addition, the EI-LMO-based electrodes present a high Coulombic efficiency (CE) of above 99.4% at 1.48 A g⁻¹ over 1000 cycles (from the 2nd cycle) and 99.8% at 148 mA g⁻¹ after 170 cycles (from the 42nd cycle), as shown in Supplementary Fig. 14c and Supplementary Fig. 14e.

## Lattice elasticity reinforced by the increased entropy

Ex situ X-ray absorption spectroscopy (XAS) measurements and analysis were conducted to investigate the impact of entropy increase on the charge compensation mechanism and local structure of LMO. In Fig. 4a, the Mn K-edge X-ray absorption near edge structure (XANES) spectra of LMO at the pristine and charged states are presented. Charging the cell containing the LMO electrode to 4.3 V, corresponding to a 100% state-of-charge (SOC), shifts its Mn K-edge XANES to the right, indicating an increase in the average oxidation state of Mn from 3.47 to 3.87, as revealed by the valence fitting (see inset). Figure 4b displays the Mn K-edge XANES spectra of EI-LMO during the first charging. At the pristine state, the oxidation state of Mn in EI-LMO is 3.56, confirming that the introduction of five low-valence cations results in an elevation of the Mn oxidation state. When charged to 4.3 V, the oxidation state of Mn increases to 3.94. The five cations (Cu^{2+}, Mg^{2+}, Fe^{2+}, Zn^{2+} and Ni^{2+}) are electrochemically inert during cycling (Supplementary Fig. 15). Multi-cation doping enhances the oxidation of Mn, thus offsetting the reduced capacity caused by inactive

elements that do not engage in charge compensation in EI-LMO. This explains why the capacity of EI-LMO at the lowest specific current (i.e., 14.8 mA g⁻¹) is nearly equivalent to that of LMO. Ex situ Extended X-ray absorption fine structure (EXAFS) measurements and analysis were conducted on LMO and EI-LMO during the initial Li metal cell charging. In Fig. 4c, d, the first peak corresponds to the Mn−O coordination shell, providing the bond lengths (Supplementary Table 4). Throughout the charging process, the Mn-O bond length of LMO decreases from 1.891 Å to 1.883 Å. In contrast, the Mn-O bond length of EI-LMO at the pristine state is 1.881 Å, shorter than that of LMO. At the 4.3 V-charged state, the Mn-O bond length is shortened to 1.878 Å, with a change of 0.03 Å, smaller than that observed in LMO (0.08 Å). This enables each Mn atom in EI-LMO to contribute more electrons for charge compensation. Consequently, the increased entropy reinforces the robustness of the Mn-O bond and enhances elasticity of the LMO lattice.

Due to the entropy-increased doping, the inhomogeneous two-phase electrochemical reaction in LMO has been mitigated, and only a solid-solution type reaction is observed in the EI-LMO, as evidenced by in situ high-resolution XRD results. Figure 4e shows the appearance of the structural transformation of LMO upon charging in two distinct stages. With the extracted Li⁺-ion amount x above 0.52, a typical two-phase transition from $Li_{0.35}Mn_2O_4$ to λ-MnO_2 is identified[43,44], as all spinel diffraction peaks suddenly have a large decrease in peak intensity and broadening of peak shape. In contrast to LMO, the structural evolution of EI-LMO is quite different (Fig. 4f); all peak offsets are smoothly distributed throughout the charging process without any peak broadening or splitting. This indicates that the electrochemical reaction within the given voltage window of EI-LMO is a single-phase solid solution reaction, indicating that the two-phase transition has been successfully mitigated.

Figure 4g and Fig. 4h illustrate the correlation between the lattice deformation and the voltage profile with the extracted Li⁺-ion amount x in LMO and EI-LMO upon cycling in Li metal coin cell configuration. As shown in Fig. 4g, when the LMO is charged to $x > 0.52$ (65% SOC), the two-phase transition implies a lattice collapse, as the two phases λ-MnO_2 and $Li_{0.35}Mn_2O_4$ coexist with a large lattice mismatch ($\Delta = 0.03$ Å). This mismatch intensifies even further ($\Delta = 0.05$ Å) when λ-MnO_2 becomes the dominant phase at a further delithiated state ($x \sim 1$). Overall, the lattice shrinks by 6.7% with a volume variation of 37.61 Å³. This lattice mismatch can lead to the formation of Mn_3O_4 phase on the surface during the initial charge. Subsequently, during the re-lithiation, Mn_3O_4 evolves into the $Li_2Mn_2O_4$ tetragonal phase, which consists of unstable Mn^{3+}-ions due to the Jahn-Teller distortion[45]. This results in Mn^{2+}-ion dissolution and surface destruction of LMO, as observed in Supplementary Fig. 16. Analysis of the ex situ XRD measurements of LMO after 500 cycles reveals a split in the (111) peak and the emergence of Mn_3O_4 peaks, and a significant amount of Mn_3O_4 peaks appear, indicating the substantial transformation of LMO into $Li_2Mn_2O_4$ and Mn_3O_4 (Supplementary Fig. 17). Additionally, the lattice deformation during discharge recovers asymmetrically compared to that during charge. In contrast, the evolution of the lattice parameter a is symmetrical throughout the charge and discharge process of EI-LMO and varies linearly with the Li content of the structure (Fig. 4d). It is also observed that the lattice parameter a of EI-LMO reduces by 0.134 Å during the full delithiation, which corresponds to a lattice shrinkage of 4.8% with a volume change of 26.72 Å³ (only ~71% of that of LMO). This surpasses exceeds the volume change exhibited by the most common Al-doped LMO[46], which experiences a volume change equivalent to 82% of that observed in LMO. Additionally, the issue of Mn^{2+}-ion dissolution is also alleviated by the entropy-increased engineering (Supplementary Fig. 16). These findings suggest a presence of a plastic deformation driven by electrochemical strain in the LMO lattice[47,48], whereas in EI-LMO, an elastic deformation is
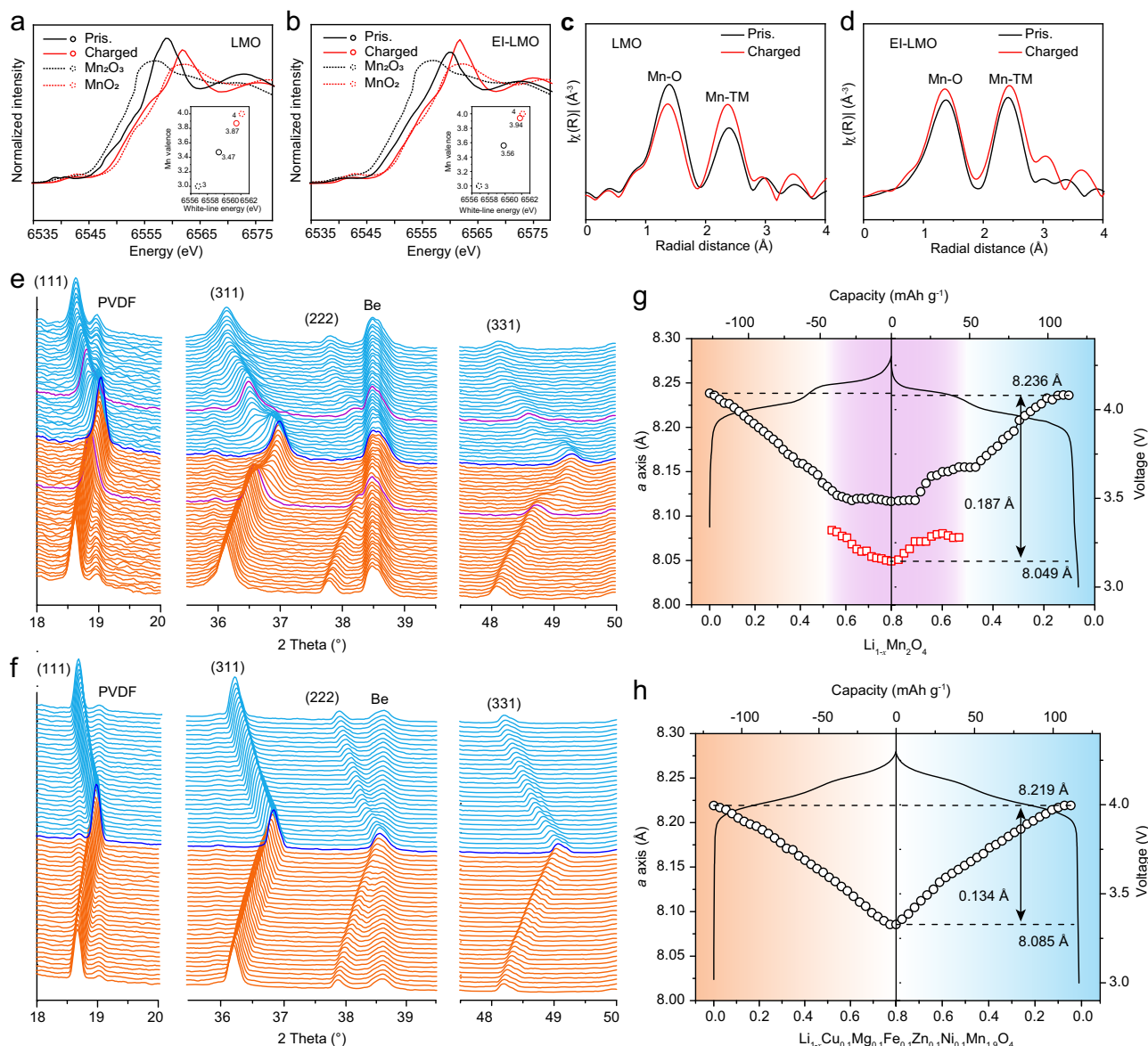
Fig. 4 | Ex situ and in situ physicochemical characterizations of LMO and EI-LMO electrodes in the first Li metal coin cell cycle at 14.8 mA g⁻¹ and 25°C. **a**, **b** Ex situ Mn K-edge XANES spectra of LMO **a** and EI-LMO **b** in pristine and 4.3 V-charged states. The 4.3 V-charged state represents the 100% state-of-charge. The insets highlight the variations in Mn valence states between the pristine and 100% SOC for both LMO and EI-LMO electrodes. **c**, **d** Ex situ Mn K-edge EXAFS spectra of

LMO **c** and EI-LMO **d** in pristine and 4.3 V-charged states (100% SOC). **e**, **f** Waterfall plots for in situ high resolution XRD of LMO **e** and EI-LMO **f**, respectively. The purple curve in **e** shows the presence of new diffraction peaks. **g**, **h** Evolutions of the lattice parameter a and the cell voltage with the lithium content in the structure of LMO (**g**) and EI-LMO (**h**), respectively. The black circles in (**g** and **h**) and red squares in (**g**) represent the $Li_{1-x}Mn_2O_4$ and λ-MnO_2 phases, respectively.

moderated by solid-solution strengthening, allowing for a mitigated and recoverable structural change due to the entropy increase effect[49].

3D channels stabilized in the solution-strengthened lattice

The mechanical responses of LMO and EI-LMO lattices to the electrochemical reaction were confirmed by ex situ STEM measurements as plastic deformation and elastic deformation, respectively. As shown in Fig. 5a, when charged to 4.3 V (100% SOC), planar defects are found and identified as {111} stacking faults in LMO[15]. The stacking faults are in the (-11-1) lattice plane, which is the close-packed plane with the lowest glide energy[50]. Geometric phase analysis (GPA) reveals that these strains are mainly concentrated on the stacking fault (Fig. 5b). Thus, LMO undergoes a plastic deformation in the form of stacking faults, to release the large and anisotropic stress created by the rapid and almost

complete delithiation. The planar defects appear as long streaks of more than 150 nm (Fig. 5c). Annular bright-field (ABF) STEM image reveals the fine structure of stacking faults (Supplementary Fig. 18), which is formed by a localized 90° in-plane tilt of the MnO₆ octahedron and an in-plane migration of Mn atoms from the 16d site to the adjacent 16c site.

In contrast, when charged to 4.3 V (100% SOC), no planar defects were observed in the HAADF STEM image of EI-LMO (Fig. 5d). The strain distribution in the delithiated EI-LMO is relatively uniform (Fig. 5e). This suggests that EI-LMO, due to the solution strengthening effect[51], mainly undergoes a moderated and elastic deformation to release the electromechanical stress, which is consistent with the single-phase solid solution transformation without significant structural changes of both O and transition metal (TM) atoms, as determined by in situ XRD. A line-scan of the image intensity shows that
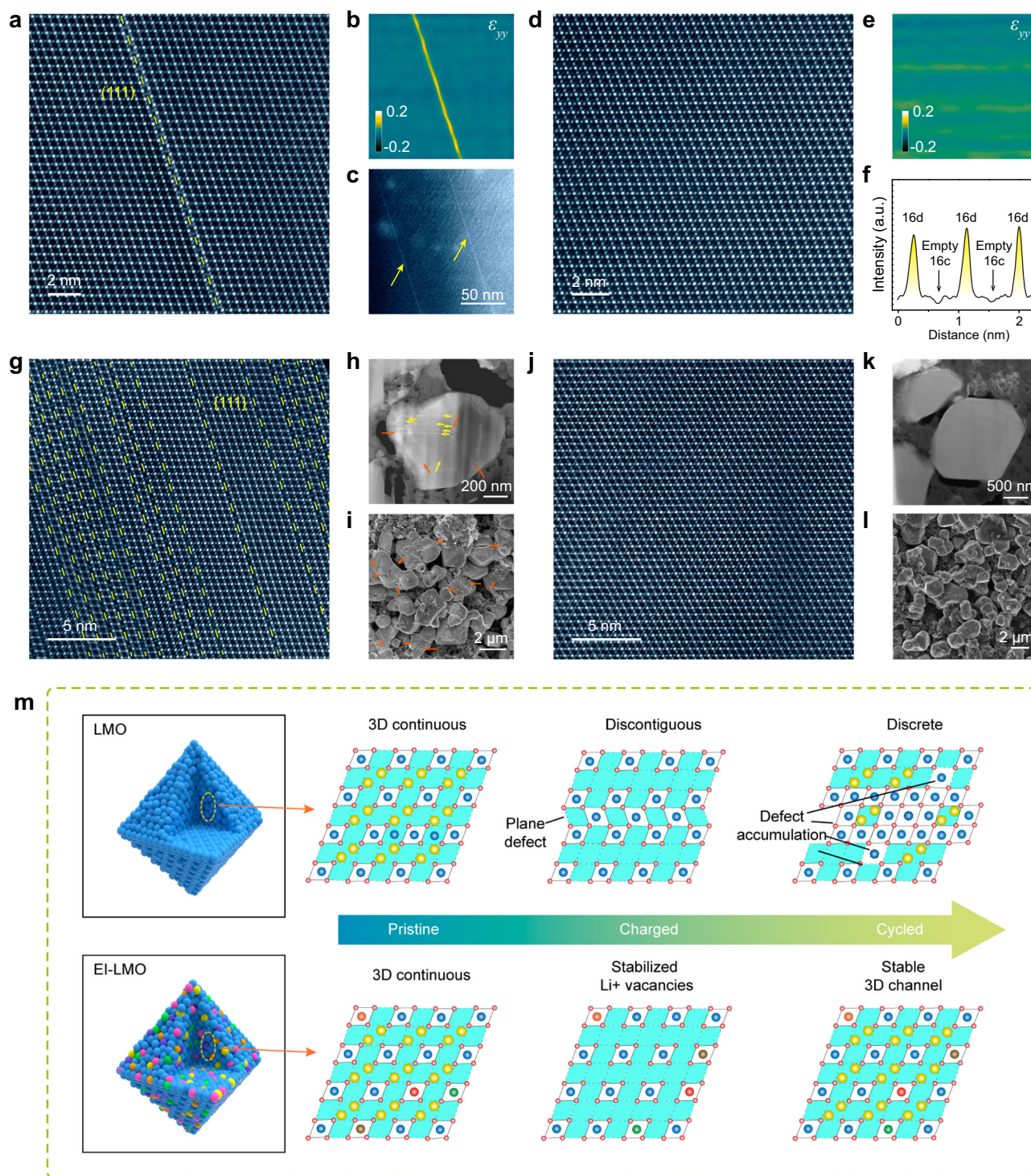
Fig. 5 | Ex situ microscopy characterizations of LMO and EI-LMO electrodes after cycling in Li metal coin cell configuration. a High magnification HAADF STEM image of LMO charged to 4.3 V (100% SOC). **b** GPA of LMO charged to 4.3 V from (**a**). **c** Cross-sectional bright-field STEM image of LMO at 100% SOC. **d** High magnification HAADF STEM image of EI-LMO charged to 4.3 V (100% SOC). **e** GPA of EI-LMO at 100% SOC from (**d**). **f** Intensity profile of the line scan along (022) plane for the demonstration of the well-preserved channel. **g** High magnification HAADF STEM image for structure analysis of LMO after 500 complete cycles at 1.48 A g⁻¹ and 25°C. **h** Cross-section bright-field STEM image for the analysis of intragranular

defects. **i** Enlarged-view SEM for the observation of the particle surface. **j** High magnification HAADF STEM image for structure analysis of EI-LMO after 500 complete cycles at 1.48 A g⁻¹ and 25°C. **k** Cross-section bright-field STEM image. **l** Enlarged-view SEM for the observation of the integrated structure of particle. **m** Schematic illustrations of the structural evolutions of the 3D channel in LMO and EI-LMO. The cyan area depicts the lithium-ion diffusion pathway, while the yellow spheres represent Li atoms, small red spheres represent O atoms, and the colored balls represent entropy-enhanced metal atoms within the structure.

there is no contrast at 16c sites (Fig. 5f), indicating that the main spinel frame structure is preserved and there is minimal diffusion of Mn-ions from 16d to 16c sites. With further characterization of the cycled samples, the plastic deformation mechanism by the {111} stacking faults was verified in the LMO-based electrodes cycled 500 times in Li metal coin cell configuration at 1.48 A g^{-1}.

As shown in Fig. 5g, there is a high density of {111} stacking faults in the cycled sample. The accumulation of repeated plastic deformation causes visible changes in the morphology of the particles, including intragranular cracks (Fig. 5h and Supplementary Fig. 19) and surface cracks (Fig. 5i). As for the cycled EI-LMO, no stacking faults, surface cracks, or intra-crystalline cracks were observed at the micron to nanometer scale (Fig. 5j–l). This suggests that the entropy-increased positive electrode is stabilized over the long-term cycling due to the elastic deformation mechanism resulting from the solution strengthening effect. As a result of the different strain release mechanisms in EI-LMO-based electrode compared to LMO, the stability of the Li$^+$-ion fast diffusion channels in EI-LMO at the fully discharged state is improved. The vacant 16c site is an essential component of the 3D Li$^+$-ion diffusion channel in the spinel structure. When this site is occupied by TM-metal ions, it disrupts the continuity of the channel. As illustrated in Fig. 5m, formation of the {111} stacking faults in LMO can lead to misplacement and discontinuity of the 3D channels (Li-8a to Mn−16c to Li-8a), due to TM-ions occupying the 16c sites. As a result, the diffusivity of Li$^+$-ions becomes sluggish at the deep charged state and cycling performance of LMO at high specific currents is largely worsened. In contrast, in EI-LMO, the integrity of the 3D channel is largely preserved, resulting in better cell cycling performance and retained high ionic diffusivity.

In summary, the co-doping of multiple transition metal elements in LMO promotes an isotropic crystalline structure in the long-range order, although the lattice is more distorted on the unit-cell scale. Entropy-increased doping leads to a more contracted lattice structure, and the mutual interactions among the elements stabilize the structure and the 3D Li$^+$-ion diffusion channels during electrochemical measurements. This enables elastic release of the electromechanical stress and smooth charge compensation during lithiation and delithiation cycles. Notably, the problematic two-phase transition from LiMn$_2$O$_4$ to λ-MnO$_2$ is effectively suppressed when the charging voltage is increased to 4.3 V. The entropy-increased doping of LMO results in improved rate capacity and cycling stability when tested in non-aqueous Li metal coin cell configuration, making it suitable for use as positive electrode active material for XFC protocols in lithium-based batteries.

Methods

Material synthesis

The pristine LiMn$_2$O$_4$ (LMO), samples doped with single-cation including LiCu$_{0.1}$Mn$_{1.9}$O$_4$ (Cu-LMO), LiMg$_{0.1}$Mn$_{1.9}$O$_4$ (Mg-LMO), LiFe$_{0.1}$Mn$_{1.9}$O$_4$ (Fe-LMO), LiZn$_{0.1}$Mn$_{1.9}$O$_4$ (Zn-LMO), LiNi$_{0.1}$Mn$_{1.9}$O$_4$ (Ni-LMO), LiTi$_{0.1}$Mn$_{1.9}$O$_4$ (Ti-LMO), LiAl$_{0.1}$Mn$_{1.9}$O$_4$ (Al-LMO), LiCr$_{0.1}$Mn$_{1.9}$O$_4$ (Cr-LMO) and LiV$_{0.1}$Mn$_{1.9}$O$_4$ (V-LMO), and the sample co-doped with five cations LiCu$_{0.02}$Mg$_{0.02}$Fe$_{0.02}$Zn$_{0.02}$Ni$_{0.02}$Mn$_{1.9}$O$_4$ (EI-LMO) samples were synthesized via a facial solid-state reaction. Stoichiometric amounts of raw materials, Li$_2$CO$_3$ (99.9%, Aladdin), MnCO$_3$ (99.9%, Aladdin), CuO (99.9%, Aladdin), Fe$_2$O$_3$ (99.9%, Aladdin), NiO (99.9%, Aladdin), MgO (99.9%, Aladdin), ZnO (99.9%, Aladdin), TiO$_2$ (99.9%, Aladdin), Al$_2$O$_3$ (99.9%, Aladdin), Cr$_2$O$_3$ (99.9%, Aladdin) and V$_2$O$_5$ (99.9%, Aladdin) were ball-milled with acetone solvent in air for 12 h at 450 rpm. Zirconia jars were 500 ml in volume, and zirconia balls with diameters of 3 mm, 5 mm, and 10 mm and the number ratio of 6:3:1 were used. The powders were dried at 120 °C overnight, then pre-sintered at 500 °C for 5 h in air in the muffle furnace and pulverized by hand-grounding using an agate mortar. The final powders were obtained by sintering at 900 °C for 18 h in Air.

Characterization

X-ray diffraction (XRD) was performed to identify the crystal structure of the synthesized samples with the 2θ range of 10°–80° (Bruker D8 Advance, Cu Kα) and step width of 0.02°. The morphology of the samples was characterized by transmission electron microscope (TEM, Talos F200s) with an accelerating voltage of 200 kV and field-emission scanning electron microscope (FE-SEM, JEOL JSM-7100F) with an accelerating voltage of 20 kV. The surface chemical information was analyzed by XPS (VG MultiLab 2000). Ex situ STEM images and EELS/EDS spectra ware performed in a CEOS probe corrected FEI Themis TEM at an electron accelerating voltage of 300 kV with a probe convergence angle of 17.8 mrad. EELS was performed with a Gatan Quantum 965 GIF system. The fine structure for the powder and cycled electrode (disassemble the coin-cell) were measured by ex situ high-energy X-ray absorption spectroscopy (XAS, Shanghai, Synchrotron Radiation Facility). The standard XAS spectral were obtained by detecting the Mn$_2$O$_3$, Mn$_3$O$_4$ and MnO$_2$ samples. The electrodes used for ex situ characterizations were dissembled from coin cells at fully charged (100% SOC) and discharged (0% SOC) states. These electrodes were subsequently washed with dimethyl carbonate (DMC, 99.9%, DoDoChem) for three times, and then dried at 25 °C for 12 h in an Ar-filled glove box (O$_2$ < 0.1 ppm, H$_2$O < 0.1 ppm). Following this, the electrodes were stored in an argon-filled sealed chamber. Before XAS and STEM measurements, the electrodes were transferred from the argon-filled sealed chamber to the sample holder with a minimal exposure to air for about one minute. For TEM and STEM analysis, the electrodes were prepared using Focus Ion Beam (FIB). For the in situ XRD experiments, a specially designed Swagelok cell equipped with an X-ray-transparent Be window was used. The in situ XRD patterns were collected with an interval of 15 min for each 2θ scan from 10 to 50° on charging and discharging at a specific current of 14.8 mA g^{-1}. The tap densities of EI-LMO and LMO are 2.21 and 2.03 g cm^{-3}, respectively. A tap density tester (Dandong Hengrui Instrument Co., HR-D1) is used to determine the tap density, with the vibration frequency set at 200 times per minute and a testing temperature of 25 °C.

Electrochemical tests

Active material, conductive carbon black (99.9% purity, ~35 nm average particle size, Guangdong Canrd New Energy Technology Co.) and polyvinylidene fluoride (PVDF, 99.5%, Guangdong Canrd New Energy Technology Co.) with the weight ratio of 90: 5: 5 were dispersed in N-methyl-2-pyrolidone (NMP, 99.9%, DoDoChem) solvent to form the slurry in Air using a high-energy Micro-Vibration Mill (MTI Co., MSK-SFM–12M). And electrodes were obtained by casting the slurry uniformly onto an Al current collector foil (99.5%, 20 μm thick, Guangdong Canrd New Energy Technology Co.) using a tape casting coater with heated vacuum bed and doctor blade (MTI Co., MSK-AFA-H200A) and the following vacuum drying at 120 °C. The mass loading of electrodes was about 4-5 mg cm^{-2}. R2032 coin-type cells were assembled in an Ar-filled glove box (O$_2$ < 0.1 ppm, H$_2$O < 0.1 ppm). The metallic lithium foil (99.9%, 0.25 mm thick, Tianqi Lithium Co.) was used as the negative electrode. And the polypropylene membrane (Celgard 2500, 25 μm thick, 0.064 μm average pore size, 55% porosity) was used as the separator. LiPF$_6$ (1 M) dissolved in a mixture of ethylene carbonate (EC), and DMC (1:1 volume ratio) with 1 wt% lithium difluoro(oxalato)borate (LiDFOB) was used as non-aqueous electrolyte solution (99.9%, H$_2$O ≤ 20 ppm, DoDoChem). A coin cell was assembled using a non-aqueous electrolyte solution with a volume of 20 μL. Galvanostatic charge−discharge cycling without current interruptions was performed using a computer-controlled battery testing system (Neware, CT-4008T). All electrochemical tests were conducted in a temperature-controlled chamber at 25 ± 3 °C. All the cycling voltage window was set between 3.0-4.3 V. The long-term cycling was conducted after two activation cycles at 14.8 mA g^{-1}, and the specific discharge capacity retention values were calculated excluding these two

activation cycles. The GITT measurements, recorded at one data point per second, were performed using the following procedure: a 10 min galvanostatic charge pulse (14.8 mA g^{-1}) was applied to the cells, followed by 30 min of relaxation time without any current being passed through the cell. The cycle, consisting of a charge pulse and a relaxation period, was applied to the cell until its voltage increased to 4.3 V. Then a discharge pulse (14.8 mA g^{-1}, 10 min) was applied to the cells, followed by a 30 min relaxation period without any current flowing through the cell. Cyclic voltammetry (CV) tests were performed on the coin cell configuration using a CHI660E electrochemical workstation. Electrochemical impedance spectroscopy (EIS) was performed using a CHI660E electrochemical workstation at 25 °C, with potentiostatic signals recorded at 38 points from 0.01 Hz to 10^5 Hz, and an amplitude of 5 mV. The open-circuit voltage of 3.4 V was maintained for 5 min before the EIS measurement.

Computational details

Ab initio calculations were performed using the VASP (Vienna Ab initio Simulation Package). For all calculations, the Perdew-Burke-Ernzerhof (PBE) generalized gradient approximation (GGA) was selected for the electronic exchange-correlation function. The energy cutoff for the plane-wave basis expansion was chosen as 600 eV. The DFT-D3 method with Becke-Jonson damping was used to correct the dispersion force. For structural optimization, the k-point mesh was up to ($3 \times 3 \times 2$) for all structures in the gamma centered Monkhorst-Pack Grid, and the maximum force tolerance was set to 0.01 eV/Å. For Electron localization function (ELF) and Bader charge calculation, the k-point mesh was up to ($4 \times 4 \times 2$) for all structures in the gamma centered Monkhorst-Pack Grid. The energy difference of 1.0×10^{-7} eV/atom was set to obtain accurate electronic ground-state calculation. For the dynamics calculation, the climbing image nudged elastic band (CI-NEB) method was carried out for the diffusion simulation, with four climbing images between initial and final states generated through the transition state tools for VASP.

Data availability

The data that support the plots in this paper and its Supplementary Information are available. All other relevant data that support the findings of this study are available from the corresponding authors on reasonable request. The source data underlying Figs. 1–5, Supplementary Fig. 2, Supplementary Figs. 4-7, Supplementary Figs. 11–15 and Supplementary Fig. 17 are provided in the Source Data file. Source data are provided with this paper.

References

1. Howell, D. et al. Enabling Fast Charging: A Technology Gap Assessment No. INL/EXT-17-41638 (US Department of Energy, 2017).
2. Liu, Y., Zhu, Y. & Cui, Y. Challenges and opportunities towards fast-charging battery materials. *Nat. Energy* **4**, 540–550 (2019).
3. Dufek, E. J. et al. Developing extreme fast charge battery protocols – A review spanning materials to systems. *J. Power Sources* **526**, 231129 (2022).
4. Yuan, M., Liu, H. & Ran, F. Fast-charging cathode materials for lithium & sodium ion batteries. *Mater. Today* **63**, 360–379 (2023).
5. Wu, M., Xu, B. & Ouyang, C. Physics of electron and lithium-ion transport in electrode materials for Li-ion batteries. *Chin. Phys. B* **25**, 018206 (2016).
6. Weiss, M. et al. Fast charging of lithium-ion batteries: a review of materials aspects. *Adv. Energy Mater.* **11**, 2101126 (2021).
7. Manthiram, A. A reflection on lithium-ion battery cathode chemistry. *Nat. Commun.* **11**, 1550 (2020).
8. Thackeray, M. M. & Amine, K. LiMn$_2$O$_4$ spinel and substituted cathodes. *Nat. Energy* **6**, 566–566 (2021).
9. Thackeray, M. M., David, W. I. F., Bruce, P. G. & Goodenough, J. B. Lithium insertion into manganese spinels. *Mater. Res. Bull.* **18**, 461–472 (1983).
10. Thackeray, M. M., Johnson, P. J., de Picciotto, L. A., Bruce, P. G. & Goodenough, J. B. Electrochemical extraction of lithium from LiMn$_2$O$_4$. *Mater. Res. Bull.* **19**, 179–187 (1984).
11. Huang, Y. et al. Lithium manganese spinel cathodes for lithium-ion batteries. *Adv. Energy Mater.* **11**, 2000997 (2021).
12. Wang, R. et al. Twin boundary defect engineering improves lithium-ion diffusion for fast-charging spinel cathode materials. *Nat. Commun.* **12**, 3085 (2021).
13. Zhang, W. et al. Kinetic pathways of ionic transport in fast-charging lithium titanate. *Science* **367**, 1030–1034 (2020).
14. Liu, H. et al. A disordered rock salt anode for fast-charging lithium-ion batteries. *Nature* **585**, 63–67 (2020).
15. Ikuhara, Y. H. et al. Atomic-level changes during electrochemical cycling of oriented LiMn$_2$O$_4$ cathodic thin films. *ACS Appl. Mater. Interfaces* **14**, 6507–6517 (2022).
16. Tang, X.-c, Huang, B.-y & He, Y.-h Determination of Li$^+$ solid diffusion coefficient in LiMn$_2$O$_4$ by CITT. *J. Cent. South Univ. Technol.* **12**, 1–4 (2005).
17. Xie, J. et al. Li-ion diffusion kinetics in LiMn$_2$O$_4$ thin films prepared by pulsed laser deposition. *Electrochim. Acta* **54**, 376–381 (2008).
18. Gludovatz, B. et al. A fracture-resistant high-entropy alloy for cryogenic applications. *Science* **345**, 1153–1158 (2014).
19. Basu, I. & De Hosson, J. T. M. Strengthening mechanisms in high entropy alloys: fundamental issues. *Scr. Mater.* **187**, 148–156 (2020).
20. Lun, Z. et al. Cation-disordered rocksalt-type high-entropy cathodes for Li-ion batteries. *Nat. Mater.* **20**, 214–221 (2021).
21. Zhang, R. et al. Compositionally complex doping for zero-strain zero-cobalt layered cathodes. *Nature* **610**, 67–73 (2022).
22. Zeng, Y. et al. High-entropy mechanism to boost ionic conductivity. *Science* **378**, 1320–1324 (2022).
23. Yeh, J.-W. Alloy design strategies and future trends in high-entropy alloys. *JOM* **65**, 1759–1771 (2013).
24. Fu, Y. et al. Synergistic enhancement effect of Al doping and highly active facets of LiMn$_2$O$_4$ cathode materials for lithium-ion batteries. *Ind. Eng. Chem. Res.* **54**, 3800–3805 (2015).
25. Li, X., Zhou, Q., Wang, H. & Liu, S. Ionothermal synthesis and enhanced electrochemical performance of nanostructure Cr-doped LiMn$_2$O$_4$ for lithium-ion batteries. *Ionics* **21**, 1517–1523 (2015).
26. Arumugam, D., Kalaignan, G. P., Vediappan, K. & Lee, C. W. Synthesis and electrochemical characterizations of nano-scaled Zn doped LiMn$_2$O$_4$ cathode materials for rechargeable lithium batteries. *Electrochim. Acta* **55**, 8439–8444 (2010).
27. Xiang, M., Su, C.-W., Feng, L., Yuan, M. & Guo, J. Rapid synthesis of high-cycling performance LiMg$_x$Mn$_{2-x}$O$_4$ (x ≤ 0.20) cathode materials by a low-temperature solid-state combustion method. *Electrochim. Acta* **125**, 524–529 (2014).
28. Zhu, J. et al. Facile synthesis of truncated octahedron LiNi$_{0.10}$Mn$_{1.90}$O$_4$ for high-performance Li-ion batteries. *Ceram. Int.* **46**, 14516–14522 (2020).
29. Liu, H. et al. On the drastically improved performance of Fe-doped LiMn$_2$O$_4$ nanoparticles prepared by a facile solution - gelation route. *Electrochim. Acta* **180**, 138–146 (2015).
30. Ding, X. et al. Electrochemical evaluation of LiAl$_{0.05}$Ni$_{0.05}$Mn$_{1.9}$O$_4$ cathode material synthesized via electrospinning method. *J. Alloy. Compd.* **632**, 147–151 (2015).
31. Yu, Y. et al. Enhancing high-rate and elevated-temperature properties of Ni-Mg co-doped LiMn$_2$O$_4$ cathodes for Li-ion batteries. *J. Colloid Interface Sci.* **555**, 64–71 (2019).
32. Yu, Y. et al. Enhancing the durable performance of LiMn$_2$O$_4$ at high-rate and elevated temperature by nickel-magnesium dual doping. *Sci. Rep.* **9**, 16864 (2019).

33. Ji, Y. et al. Improved capacity retention and ultralong cycle performance of Ni-Fe co-doped LiMn$_2$O$_4$ cathode material at high current densities. *Colloids Surf. A* **648**, 129259 (2022).

34. Shi, J.-L. et al. Size controllable single-crystalline Ni-rich cathodes for high-energy lithium-ion batteries. *Natl Sci. Rev.* **10**, nwac226 (2023).

35. Jiang, N. & Spence, J. C. H. Interpretation of oxygen K pre-edge peak in complex oxides. *Ultramicroscopy* **106**, 215–219, (2006).

36. Huang, Z.-F. et al. Tuning of lattice oxygen reactivity and scaling relation to construct better oxygen evolution electrocatalyst. *Nat. Commun.* **12**, 3992 (2021).

37. Tanim, T. R. et al. Enabling extreme fast-charging: challenges at the cathode and mitigation strategies. *Adv. Energy Mater.* **12**, 2202795 (2022).

38. Zhang, W. et al. Lowering charge transfer barrier of LiMn$_2$O$_4$ via nickel surface doping to enhance Li$^+$ intercalation kinetics at subzero temperatures. *J. Am. Chem. Soc.* **141**, 14038–14042 (2019).

39. Guo, Z. et al. Ultrafast non-equilibrium phase transition induced twin boundaries of spinel lithium manganate. *Adv. Energy Mater.* **14**, 2302484 (2024).

40. Tan, G., Wan, S., Chen, J.-J., Yu, H.-Q. & Yu, Y. Reduced lattice constant in Al-doped LiMn$_2$O$_4$ nanoparticles for boosted electrochemical lithium extraction. *Adv. Mater.* **36**, 2310657 (2024).

41. Zhu, W. et al. Ultrafast non-equilibrium synthesis of cathode materials for Li-ion batteries. *Adv. Mater.* **35**, 2208974 (2023).

42. Yang, S. et al. Surface magnesium substitution at spinel lithium manganate 8a tetrahedral sites for suppressed manganese dissolution and enhanced cycle stability. *ACS Energy Lett.* **8**, 4278–4286 (2023).

43. Berg, H., Rundlöv, H. & Thomas, J. O. The LiMn$_2$O$_4$ to λ-MnO$_2$ phase transition studied by in situ neutron diffraction. *Solid State Ion.* **144**, 65–69 (2001).

44. Berg, H. & Thomas, J. O. Neutron diffraction study of electrochemically delithiated LiMn$_2$O$_4$ spinel. *Solid State Ion.* **126**, 227–234 (1999).

45. Liu, T. et al. Correlation between manganese dissolution and dynamic phase stability in spinel-based lithium-ion battery. *Nat. Commun.* **10**, 4721 (2019).

46. Zhang, S. et al. Atomically interlocked chemistry activated by interstitial sites in LiMn$_2$O$_4$ cathode. *Adv. Funct. Mater.* **33**, 2210731 (2023).

47. Zeng, K. & Zhu, J. Surface morphology, elastic modulus and hardness of thin film cathodes for Li-ion rechargeable batteries. *Mech. Mater.* **91**, 323–332 (2015).

48. Stallard, J. C. et al. Mechanical properties of cathode materials for lithium-ion batteries. *Joule* **6**, 984–1007 (2022).

49. Bi, Y. et al. Reversible planar gliding and microcracking in a single-crystalline Ni-rich cathode. *Science* **370**, 1313–1317 (2020).

50. Yuan Lu, J. W. H. X. First-principles study on low index surface structure optimization and surface energy of LiMn$_2$O$_4$ spinel oxides. *Acta Chim. Sin.* **79**, 1058–1064 (2021).

51. Zhang, S. et al. Element substitution of a spinel LiMn$_2$O$_4$ cathode. *J. Mater. Chem. A* **9**, 21532–21550 (2021).

Acknowledgements

Author contributions

W.Z., J.Y., S.M. and J. Wu proposed the research and conceptualized the idea. W.Z. and J. Wang synthesized all the samples and performed the electrochemical measurements and SEM characterization. W.Z., F.X. and J. Wu collected the TEM characterizations and analyzed data. H.P. performed DFT calculations. W.S. and J.Y. conducted the in situ electrochemical XRD tests. W.Z., F.X., H.P., J.Y., Q.L., H.W., G.W., S.M. and J. Wu participated in data analysis and discussion. W.Z., S.M. and J. Wu drafted the manuscript with input and revision from all authors.

Competing interests

The authors declare no competing interests.

Additional information

Supplementary information The online version contains supplementary material available at https://doi.org/10.1038/s41467-024-51168-1.

Correspondence and requests for materials should be addressed to Shichun Mu or Jinsong Wu.

Peer review information *Nature Communications* thanks Dibyendu Bhattacharyya, Juan Carlos Gonzalez-Rosillo, and Wei Kong Pang for their contribution to the peer review of this work. A peer review file is available.

Reprints and permissions information is available at http://www.nature.com/reprints

Publisher's note Springer Nature remains neutral with regard to jurisdictional claims in published maps and institutional affiliations.